Published in final edited form as:

Brain Struct Funct. 2018 April ; 223(3): 1107–1120. doi:10.1007/s00429-017-1541-9.

Morphological determinants of dendritic arborization neurons in *Drosophila* larva.

Sumit Nanda[1], **Ravi Das**[2], **Shatabdi Bhattacharjee**[2], **Daniel N. Cox**[2], **Giorgio A. Ascoli**[1,*]

[1]Center for Neural Informatics, Structures, & Plasticity, Krasnow Institute for Advanced Study, George Mason University, Fairfax, VA, USA

[2]Neuroscience Institute, Georgia State University, Atlanta, GA, USA

Abstract

Pairing *in vivo* imaging and computational modeling of dendritic arborization (da) neurons from the fruit fly larva provides a unique window into neuronal growth and underlying molecular processes. We image, reconstruct, and analyze the morphology of wild type, RNAi-silenced, and mutant da neurons. We then use local and global rule-based stochastic simulations to generate artificial arbors, and identify the parameters that statistically best approximate the real data. We observe structural homeostasis in all da classes, where an increase in size of one dendritic stem is compensated by a reduction in the other stems of the same neuron. Local rule models show that bifurcation probability is determined by branch order, while branch length depends on path distance from the soma. Global rule simulations suggest that most complex morphologies tend to be constrained by resource optimization, while simpler neuron classes privilege path distance conservation. Genetic manipulations affect both the local and global optimal parameters, demonstrating functional perturbations in growth mechanisms.

Keywords

Neuronal Development; Molecular Neurogenetics; Confocal Microscopy; Morphological Reconstructions; Computational Modeling

Introduction

The diversity of dendritic morphology among neuron types affects neuronal connectivity, synaptic integration, and neuronal excitability (Mainen and Sejnowski 1996; Vetter et al. 2001; London and Häusser 2005; Bird and Cuntz 2016). Given such functional and computational relevance, the fine regulation of dendritic arbor development by a multitude of intracellular, extracellular, and activity-dependent cascades (Jan and Jan 2010) is not surprising. However, how the exuberant complexity and variability in mature arbors emerges from class-specific convergence of these numerous mechanisms on the immediate molecular mediators of dendritic growth remains largely unknown (Ascoli 2002; Gao 2007).

*Correspondence: ascoli@gmu.edu, phone: (703) 993-4383.

The sensory dendritic arborization (da) neurons from the larva peripheral nervous system (PNS) of *Drosophila melanogaster* constitute a powerful experimental system to study class specific dendritic development, including branching, elongation, global-scaling, tiling, and remodeling (Parrish et al. 2007; Corty et al. 2009; Singhania and Grueber 2014; Tavosanis 2014; Couton et al. 2015). This animal model offers multiple advantages: it is genetically tractable, enabling both seamless fluorescent tagging and molecular manipulations; the neurons lie beneath a transparent cuticle, allowing straightforward *in vivo* optical microscopy; the relatively rapid larva-to-adult metamorphosis implies substantial structural dynamics over a contained temporal period; and readily identifiable neurons are reliably found in stereotypical anatomical locations across animals. Fruit fly da neurons are categorized into four well-defined morphological classes (I-IV) with increasing dendritic size and complexity (Fig. 1, 2a). Dendrites of Class I and II neurons exhibit selective coverage of the body wall, whereas Class III and IV neurons exhibit largely complete and non-overlapping dendritic coverage of the body wall, and display dendritic tiling via homo-neuronal repulsion (Grueber et al. 2002). Each morphological class can be further divided into subtypes based upon their locations along the dorsal-ventral axis of the animal and the dendritic territories their arbors cover (e.g. dorsal, lateral, ventral domains). Moreover, at a molecular level, studies have demonstrated that even within a subclass (e.g. Class IV da neurons), different genetic programs operate in regulating subtype specific dendritic architecture (Iyer et al. 2013).

Distinct computational methods exist for studying dendritic morphology and development. In segmental rate models, dendrites grow out of the soma in a time-dependent manner and the dynamics of growth cones present at the branch terminals regulate branch bifurcation and extension (van Pelt and Schierwagen 2004). This type of stochastic simulation is not generally informed by real tree morphometrics, but can reproduce the observed variability in dendritic terminals from various neuron types (van Pelt and Uylings 2002) and is suitable to create large-scale networks of realistic neuronal morphology (Koene et al. 2009).

Data driven models constitute an alternative computational framework focusing on the outcome of dendritic growth rather than the dynamic process of development. This approach integrates simulations with experimental data to quantify the consequences of hypothesized sub-cellular interactions of local molecular cues controlling structural development. This method is thus complementary to traditional qualitative observations and morphometric quantifications. In particular, local rule-based stochastic models fit growth parameters measured from real neurons to statistical distributions and resample them to generate virtual dendrites (Burke et al. 1992; Uemura et al. 1995; Ascoli and Krichmar 2000; Donohue and Ascoli 2008). Global rule-based simulations, in contrast, implement fundamental wiring constraints to optimize the long-theorized balance between resource conservation and conduction time (Ramón y Cajal 1995; Cuntz et al. 2010). Surprisingly, computational simulations have never been used in the experimentally conducive system of da neurons in the fly larva PNS.

Here we image, reconstruct, and openly share different classes of dendritic arborization neurons, and complement this new dataset with previously available digital tracings (Sulkowski et al. 2011; Wang et al. 2013) from NeuroMorpho.Org (Ascoli et al. 2007). We

then measure dendritic arbor size and complexity across neuronal classes. Using the *GAL4/UAS* binary expression system, we disrupt specific *Drosophila* genes in Class IV da neurons by RNA interference (RNAi) and digitally reconstruct and analyze the altered morphologies of these neuronal subtypes. We then apply the aforementioned local rule-based (Donohue and Ascoli 2008) and global rule-based (Cuntz et al. 2010) models to simulate artificial dendritic morphologies for all wild type (WT) and genetically altered neuron groups. The optimal parameters we identify for each simulation strategy reveal distinct morphological determinants of mature dendritic arbors. Finally, we compare these results to those obtained with a complementary segmental rate outgrowth simulation (van Pelt et al. 1997).

Materials and Methods

All analyzed da neuron morphologies were either reconstructed for this study (N=127) or downloaded from the Cox (N=67) and Ye (N=5) archives of NeuroMorpho.Org. Specifically, the complete dataset studied here consists of the following cells: 25 Class I ddaD (21 new, 4 Cox) and 25 Class I ddaE (21 new, 4 Cox); 18 (Cox) Class II (2 ddaB, 4 ldaA, 6 vdaA, 6 vdaC); 9 new Class III (8 vdaD, 1 v'pda) and 25 from Cox (7 ddaA, 5 ddaF, 5 ldaB, 4 vdaD, 4 v'pda); 34 wild type Class IV (13 new ddaC, 5 Ye ddaC, 6 Cox ddaC, 7 Cox v'ada, 3 Cox vdaB); and 63 new mutant Class IV (7 *RpS2-IR*, 6 *RpS13-IR*, 6 *RpS17-IR*, 12 *Ank2-IR*, 12 *RhoGAP18B-IR*, 9 *wdb-IR*, 11 *SkpA-IR*). Unless otherwise noted, neuronal subtypes were pooled within each morphological class. All newly reconstructed cells will be freely available through the Ascoli and Cox archives of NeuroMorpho.Org.

The fluorescently labeled da neurons of wild type (Class I, Class II, Class III, and Class IV) and RNAi-knockdown phenotypes (Class IV only) were imaged via *in vivo* confocal microscopy using a previously published protocol (Iyer et al. 2013). To visualize the dendritic membrane, the following *GAL4-UAS* recombinant transgenic strains were used: $GAL4^{221}$,*UAS-mCD8::GFP* (Class I; Grueber et al. 2003); $GAL4^{GMR37B02}$,*UAS-mCD8::GFP* (Class II; Turner et al. 2016); $GAL4^{19-12}$,*UAS-mCD8::GFP* (Class III; Xiang et al. 2010); and $GAL4^{477}$,*UAS-mCD8::GFP; ppk-GAL4,UAS-mCD8::GFP* (Class IV; Iyer et al. 2013). In brief, for live confocal analyses, larvae were placed on a microscope slide, immersed in 1:5 (v/v) diethyl ether to halocarbon oil and covered with a 22×50 mm glass coverslip. Neurons expressing fluorescently tagged markers were visualized on a Zeiss LSM 780 confocal microscope with a 20X dry objective (420650–9901 Plan Apo M27, NA 0.8) and 1 Airy Unit for the pinhole. Images were collected as z-stacks at a step-size of 1.0–2.0 μm and 1024×1024 resolution. Altering the step sizes affected only slightly the overall morphometric measurements, and these differences were negligible relative to cell type specific morphological differences (See Suppl. Fig. 3). Neurons from a specific cell group were imaged at fixed step size. Increasing the objective magnification from 20X to 63X did not reveal any additional thin dendritic branches (See Suppl. Fig. 2). Gene-specific *UAS-RNAi* transgenic lines (IRs) were obtained from the TRiP collection at the Bloomington stock center (NIH P40OD018537) and two independent lines were tested for each gene, wherever possible. These transgenic strains include: 53319 (*UAS-RpS2-IR*); 34820 (*UAS-RpS13-IR*); 42656 (*UAS-RpS17-IR*); 33414 (*UAS-Ank2-IR*); 31165 (*UAS-RhoGAP18B-IR*); 38950 (*UAS-wdb-IR*); and 32991 (*UAS-SkpA-IR*). Representative images and

reconstructions were performed using these RNAi transgenes, which produced consistent phenotypes.

Image stacks were manually reconstructed in Vaa3D (Peng et al. 2014) and edited in NeuTube (Feng et al. 2015). Branch thickness was estimated automatically using the neuron radius plug-in of Vaa3D. The program computes the local diameter of each tracing node based on the planar (X-Y) spread of the signal with an intensity threshold of 15 on a 0–255 scale. Further topological errors were programmatically resolved using TREES Toolbox (Cuntz et al. 2010). Morphometric analyses were carried out with L-Measure (Scorcioni et al. 2008). For quantification of morphological homeostasis, individual trees were stochastically recombined in the MATLAB environment (MathWorks, Natick, MA).

The local rule-based model of artificial tree generation followed the same algorithm previously designed for vertebrate neurons (Donohue and Ascoli 2008; Java code publicly available at senselab.med.yale.edu/modeldb with accession number 114310). In brief, five basic morphological parameters (1. taper rate; 2. the diameter ratio between the parent branch and the thicker daughter branch; and 3. the diameter ratio between the two daughter branches; 4. branch path length; and 5. probability of bifurcation) were measured from each group of real neurons. Each parameter was binned by three fundamental determinants (FDs): local radius, branch order, and path distance from the soma. Here branch order is classically defined as the number of bifurcations along the path to the soma and is distinct from the Strahler number (Strahler 1953; Uylings et al. 1975). The measured data in every bin were then reduced to statistical distributions selected for each case as the best fits among Gaussian, uniform, and gamma functions. Next, the five basic parameters (BPs) were randomly sampled from each of the relevant bins (based on the current radius, branch order or path distance from soma) using a recursive tree generation algorithm. Out of the three fundamental determinants, branch radius is the one potentially most sensitive to the imaging resolution. However, the majority of the measured dendritic thickness values in the fly larva da neurons lie above the diffraction limit of light microscopy. Each of the five BPs was constrained by one of the three FDs, creating a total of 3^5 or 243 model variants. We then selected the ten variants that best matched the total number of bifurcation, total surface area, bifurcation asymmetry, and surface asymmetry (Donohue and Ascoli 2008) measured from the corresponding real cell group. As overall measure of statistical proximity between each model variant and the real data, we averaged the four Welch test t-scores (Welch 1947).

In the global rule based simulation (Cuntz et al. 2010), the artificial dendritic arbor shape is constrained by the “density profile” of a neuron group and by a balancing factor (bf) that weighs two demands: the minimization of resource and the minimization of conduction time. Higher bf values correspond to increased importance of conduction time minimization relative to resource minimization and vice versa. The global simulation was carried out using the TREES Toolbox package (Cuntz et al. 2010) in the MATLAB environment (v1.15, code freely available at treestoolbox.org). Each neuron was resampled at 1 μm inter-nodal distance before generating the artificial trees. Eleven different balancing factors from 0 to 1 were used in steps of 0.1.

To identify the best performing local and global model parameters for each cell class, we used the distributions of dendritic length against path distance from soma and of number of tips against branch order as selection criteria. Specifically, for each of these two curves, we averaged over all data points the absolute difference between a real neuron group and each of the corresponding artificial groups. If the (real and simulated) distributions consist of n data pair points X_i, Y_i {\displaystyle (x_{i},y_{i})\!}($i = 1 \ldots n$), where ***{\displaystyle x_{i}\!}X_i*** is either branch order or path distance and ***{\displaystyle y_{i}\!}Y_i*** is either number of tips or total length, then we calculate ***S*** for each curve as

$$S = \sum_{i=1}^{n} \mathbf{abs}(Yir - Yis) / \sum_{i=1}^{n} Yir$$

Where ***Yir*** is real and ***Yis*** is simulated. The averages of the two S values were used to rank the top local and global model variants. The results from the best parameter(s) for each neuron group are displayed in the Results (Fig. 4, 5, 6 and Table 1).

For the simplest (Class I) and the most complex (Class IV) neuron types, we also implemented as an alternative the 'BE' model (van Pelt et al. 1997). In this approach, the dynamic behavior of the growth cones is time-dependent and defined by two parameters: the expected number of bifurcation events on a branch (B) and the influence of the total number of terminal at any given time on bifurcation probability (E). These two parameters represent respectively the intrinsic drive for branching and the competition among growth cones for cellular resources. We programmed the BE model in the Matlab environment and identified the optimal parameters B and E values for three wild-type (Class I, Class III and Class IV) and two genetically altered (*UAS-RpS2-IR* and *UAS-SkpA-IR*) neuron types.

Results

Dendritic arborization (da) neurons are highly diverse in branching complexity, area covered, and overall shape. Neuronal images and reconstructions from all classes of WT da neurons, as well as three RNAi Class IV ddaC neuronal reconstructions (showing substantially reduced, slightly increased, and relatively unchanged examples of mutant phenotypes) are represented in Fig. 1. These characteristics can be operationally quantified in terms of total arbor length and number of terminal tips as well as of the distribution of those two measures across the arbors, reflecting the amount and allocation of used resources. The distributions of dendritic length over path distance exhibit significant differences among morphological classes, consistent with previous studies (Grueber et al. 2002). Class IV neurons are the most complex, and Class I neurons are the simplest; Class II and Class III neurons have intermediate levels of size and complexity (Fig. 2a). Within Class IV, subtypes ddaC, v'ada, and vdaB differ slightly from each other (Fig. 2a inset). The ddaC phenotypes in which genes were disrupted using RNA interference (RNAi) with inverted repeats also show considerable morphological diversity (Fig. 2b). These genes were selected for analyses based upon neurogenomic investigations that identified putative downstream effectors of the Cut and/or Knot transcription factors, which regulate class-specific patterns of da neuron dendrite morphogenesis (Grueber et al. 2003; Jinushi-Nakao et al. 2007). Of the seven

RNAi-knockdown phenotypes reconstructed here, three (*Ank2-IR*, *RhoGAP18B-IR* and *wdb-IR*) are very similar and show slightly reduced complexity, with a distal shift in peak length distribution relative to wild type (Fig. 2b top inset). Three others (*RpS2-IR*, *RpS13-IR*, and *RpS17-IR*) show dramatically reduced arbor complexity (Fig. 2b bottom inset). In contrast, RNAi-knockdown of *SkpA* (*SkpA-IR*) shows increased complexity relative to wild type.

All wild type da neuron classes demonstrate intrinsic structural homeostasis (Samsonovich and Ascoli 2006), where an increase in size and complexity in one of the dendritic stems is compensated by the other dendritic stems within the same neuronal arbor (Fig. 3). Class I neurons have two or three stems emerging from the soma (Fig. 3b), while Class IV neurons can have one to five stems (Fig. 3e). As the number of stems (in both Class I and Class IV) per neuron increases, the average size (total length) and complexity (total number of tips) of the sub-trees pertaining to each stem decrease (Fig. 3b, 3e). The same results were observed in Class II and Class III da neurons (not illustrated). This is consistent with the notion of neurons growing until they reach a certain total length and number of branches independent of the number of stems among which the cable is distributed. To evaluate whether this homeostatic behavior could be observed at the tree-by-tree level within neurons, we virtually shuffled the dendritic stems in all possible combinations among neurons with the same number of stems. We then grouped these virtual neurons randomly (each group containing equivalent number of neurons to the real group) and calculated the standard deviation of the total neuron length for each group. The standard deviation of the real Class I neuron group is substantially lower than all of the corresponding virtual groups (Fig. 3c), and the same holds true for Class II and Class III neurons (not illustrated). In contrast, the standard deviation of real Class IV group lies close to the middle of the histogram (Fig. 3f). Thus, while da neurons in Classes I-III demonstrate morphological homeostasis both at the whole-cell level and on a tree-by-tree basis, Class IV neurons only tend to balance overall size by compensating for the variable number of trees. This distinction is also corroborated by the higher variability among trees within Class IV relative to the other three classes (coefficient of variation for total length in Class IV neurons: 0.28, compared to 0.23 for Class I).

In light of the demonstrated morphological homeostasis, we opted to model the entire arborization of each individual neuron instead of the individual subtrees separately. After generating artificial neurons using all the model variants, we compare two distributions that represent size (dendritic branch length against path distance from soma) and complexity (number of tips against branch order), between each artificial group and the corresponding real neuron group. We then select the variant that overall approximates the two real distributions best as the optimal model variant for that neuron type. We assume that the parameters (or a single parameter in case of the global model) that make up the top performing model variant is representative of the biological growth rules that establish the size and shape of that neuron type. For example, the model variant that best fits Class IV neuron group is 75_ PD_BO_BO_PD_BO (Fig. 4 e, f, g, h), which describes that it is the 75^{th} (out of 243) local variant where the five basic parameters (1) taper rate, (2) parent-daughter ratio, (3) daughter ratio, (4) branch path length and (5) bifurcation probability are best determined by path distance from soma, branch order, branch order, path distance from soma, and branch order respectively. The model that best fits Class I neurons is

3_PD_PD_PD_PD_BO (Fig. 4 a, b, c, d), where all basic parameters are best determined by path distance from soma, except bifurcation probability, which is determined by branch order. Analyzing the determinants of the two main basic parameters (branch path length and probability of bifurcation) reveal that for all the WT da neuron groups, branch order is the best determinant of bifurcation probability (Fig. 4, Table 1). Branch path length is best constrained by path distance from the soma in WT Class I, III and IV neurons, whereas for Class II neurons, branch order is a better constraint (Table1 and Fig. 4). Overall, path distance from the soma has a greater influence on Class I (Fig. 4 a, b, c, d), and branch order on Class IV (Fig. 4 e, f, g, h). Four of the five basic parameters for Class I are most affected by path distance from the soma (Fig. 4 a, b, c, d), and three of the five basic parameters in Class IV are best constrained by branch order (Fig. 4 e, f, g, h).

In global-rule based simulation, randomly generated points within the average spread of a neuron group are connected using a minimum spanning tree algorithm, where the single bf parameter balances the relative influence of wiring minimization (or minimization of cytoplasmic resource) and conduction time minimization (or minimization of path distance from root to each point of interest). Increasing the balancing factor gradually increases the relative influence of conduction time minimization (Cuntz et al. 2010). Analyzing the best global variants shows that Class I artificial neurons are best generated using a balancing factor of 0.6 (Fig. 5 a, b, c, d), whereas for Class IVs the optimal balancing factor is 0.3 (Fig. 5 e, f, g, h). This indicates that the demand of conduction time (path distance minimization) is more influential for Class I, which is consistent with their selective innervation property. In contrast, the importance of resource optimization is greater in Class IV neurons, consistent with their space filling nature that puts substantial demands on wiring minimization.

Next we analyze RNAi knockdown phenotypes for genes that either severely reduce (*RpS2-IR*) or augment (*SkpA-IR*) Class IV (ddaC) dendritic complexity relative to WT controls. In the optimal local model for *RpS2-IR* (204_BO_RD_RD_RD_BO, Fig. 6 d, Table 1), branch radius, which is correlated with microtubule density (Hillman, 1979; Brill et al. 2016), determines branch path length in addition to two other basic parameters. However, branch order is still a better predictor of bifurcation probability (Fig. 6 c, d, e, and f; Table 1). In the global model, a balancing factor of 0.2 generates the optimal artificial *RpS2-IR* neuron morphology (Fig. 6 a, b, e, f, Table 1), suggesting a greater need for resource optimization in this phenotype than in WT. In contrast, both probability of bifurcation and branch path length of artificial ddaC neurons from *SkpA-IR* are optimally constrained by branch order (Fig. 6 i, j, k, l; Table 1), indicating that the distribution of resource is the primary determinant of size and complexity in this mutant. The optimal balancing factor in global simulation of the *SkpA-IR* dendritic phenotype was 0.3, the same value as in WT (Fig. 6 g, h, k, l). The average total length and number of tips along with the optimal local and global simulation parameters for all other neuron groups, including Class II, Class III, and the remaining RNAi knockdowns are included for completeness in Table 1.

Finally, we use a segmental rate outgrowth model (van Pelt et al. 1997) to describe the distribution of terminals for both wild-type (Class I, Class III and Class IV) as well as genetically altered (ddaC *SkpA-IR* and *RpS2-IR*) da neurons. This framework does not

make use of the local information of branch order, path distance, and radius. The dynamic behavior of the growth cones is instead time-dependent and influenced by two parameters (see Methods). As expected, we observe a progression in the expected number of bifurcations (parameter B) from simpler to more complex da neurons (Suppl. Fig. 1 a, b, c, d, e). The higher variability in number of terminals for Class III da neurons (when compared to Class I da neurons as described earlier and in Suppl. Fig. 2 b and f) can be reproduced by reducing the influence of the number of existing terminals at any given time on branching probability (parameter E). Interestingly, the relationship between the average branch order of all branches and parameter B depends on partition asymmetry (Suppl. Fig. 1 f) due to the influence of short terminal branches. Parameter B is higher than the average branch order in symmetric tree structures (Class I, Class IV and ddaC *SkpA-IR*), lower for ddaC *RpS2-IR*, and much lower for Class III da neurons, which have many short terminals branches and is highly asymmetric.

Discussion

Complex and varied molecular processes are involved in the dendritic development of different cell types, leading to diverse class-specific morphologies (Nguyen et al. 2004). This exquisitely controlled variation in dendritic shape is in turn highly relevant in nervous system functioning, due to its profound effects on synaptic integration, neuronal excitability, and circuit connectivity. Comparative studies of da neurons can aid the discovery of crucial elements directing the growth and maintenance of class-specific neuronal arborizations. The convenient anatomical position of these dendritic arbors underneath a thin, translucent cuticular epithelium facilitates high-resolution live cell imaging, and the highly advanced genetic tools available in the fruit fly system allow for sophisticated investigation of molecular and neural functions.

Extensive investigations have uncovered numerous genetic and cellular systems that direct class-specific dendrite growth. These include transcriptional regulation, cell signaling pathways, endocytic and secretory pathways, modulation of cytoskeletal proteins, RNA targeting and local translation, and activity-dependent plasticity of dendritic structure (Jan and Jan 2010; Tavosanis 2014). In this study and for the first time in da neurons, we use computational modeling in parallel with experimental molecular perturbations.

The morphometric analyses in this study highlight the inter-class and inter-subclass variability in dendritic size among da neurons (Fig. 2a). We also observe subtle as well as drastic changes in dendritic size for genetically altered ddaC morphologies (Fig. 2b). Disruptions of the small ribosomal subunits encoding genes *RpS2, RpS13*, and *RpS17* leads to severe reductions in Class IV dendritic complexity suggesting that these neurons are highly sensitive to impairment of ribosomal function. Defects in cytoskeletal regulatory molecules *Ankyrin2* (*Ank2*) and *RhoGAP18B*, as well as the PP2A phosphatase complex regulatory subunit *widerborst* (*wdb*) lead to alterations in branching architecture with reduced proximal arborization near the soma, in favor of a distal shift in peak length distribution resulting in clustered short terminal branching. Finally, defects in the ubiquitin ligase complex subunit *SkpA* lead to excessive arborization, indicative of a role for ubiquitin proteasomal degradation in restricting arborization complexity.

We demonstrated that dendritic size (in total length) and complexity (in total number of tips) in da neurons are under intrinsic homeostatic regulation, where fluctuations in one tree of a neuron are compensated by the other trees (Fig. 3b, 3e). We also observe this behavior at the tree-by-tree level for Classes I, II, and III (but not IV), whereas the inter-neuron variability of real neurons is markedly lower than would be expected if trees were assembled independently among somata (Fig. 3c, 3f).

Our observations in da neurons are consistent with structural homeostasis observed in the mammalian cortex (Samsonovich and Ascoli 2006). In mammals, regular electrophysiological activities are also sustained through homeostatic mechanisms that adapt synaptic strengths to maintain functional stability (Turrigiano and Nelson 2004), even when animals were exposed to chronic psychosocial stress (Kole et al. 2004). Moreover, previous studies in *Drosophila* have shown that dendritic arbors can adjust their structure in response to the level and distribution of their received inputs (Tripodi et al. 2008).

The local rule-based simulation used in this study is essentially a mixture of several models. Historically three fundamental determinants have been proposed to locally constrain growth: branch radius, branch order, and path distance from the soma (Donohue and Ascoli 2008). These three determinants closely approximate actual biological processes. Radius can be correlated with the density of microtubules (Hillman 1979; van Beuningen et al. 2015) and has been used to simulate real-like features of dendritic growth in several neuron types (Burke et al. 1992; Donohue and Ascoli 2005). Branch order indexes the split of cytoplasmic resources at each bifurcation and has been employed to model the distribution of morphological properties in many simulation systems (Uemura et al. 1995; van Pelt et al. 1997). Path distance from the soma alters the time required for intracellular signaling and transport, both to and from the soma, and was found to appropriately constrain the artificial growth of spinal motor neurons and hippocampal pyramidal cells (Burke et al. 1992; Samsonovich and Ascoli 2005).

From the simulations presented here we observe that the probability of bifurcation is best determined by branch order in all wild type da neurons. This finding indicates that these neurons may have the capacity to determine the amount of available cytoplasmic resource locally after each bifurcation. Path distance from soma generally performs better in constraining branch path length, implying that distance and time required for subcellular transport may affect the length of dendritic branches.

Neurons have finite amounts of cytoskeletal resources to approximate the ideal shape and topology best suited for their functional role in the circuit. The global simulation assumes that the demand of a desired morphology determines how the cytoskeletal resources are distributed during dendritic outgrowth and branching (Cuntz et al. 2010). In our global simulation, raising bf from 0 to 1 in 0.1 steps gradually increases the relative influence of conduction time minimization while reducing the relative demand for resource minimization. A lower balancing factor usually leads to a more branched structure, where the neuron tries to utilize its cytoskeletal resources to the fullest, to fill up a large space. With a higher balancing factor, there are fewer bifurcations as each point of input (for

example, spines or regions of direct sensory reception) demand a relatively direct connection with the soma.

Our local model results demonstrate that Class I neurons are overall more influenced by path distance from the soma, which controls four of the five basic parameters of top local model variant (3_PD_PD_PD_PD_BO). This observation is consistent with the results of the global simulations, in which the virtual Class I neurons are better generated with a higher balancing factor (0.6), which signifies conduction time minimization. Altogether, these results indicate a greater emphasis on path distance minimization, and is consistent with the selective innervation characteristic of Class I neurons. Class IV neurons in contrast are space-filling multisensory neurons with tiling properties. Naturally, these highly branched structures have tremendous cytoplasmic resource demands and hence are best generated in global simulation at a lower balancing factor (0.3), and with branch order overall exerting greater influence in local simulation.

RpS2-IR ddaC neurons have significantly reduced complexity, and their branch path lengths are best determined by radius. This may be caused by lower levels of microtubules in these mutants, which correlates with branch diameter (Burke et al. 1992; van Beuningen and Hoogenraad 2016). The *RpS2* morphological phenotype is also best approximated in global simulations with the slightly lower bf of 0.2, possibly revealing a greater need to conserve resources than wild type. These simulation findings are well aligned to the functional role of RpS2 as a component of the small ribosomal subunit. A disruption in ribosomal function could negatively impact protein translation leading to limited resources, including cytoskeletal building blocks such as α- and β-tubulin needed for microtubule assembly. *SkpA-IR* ddaC neurons have increased complexity, and both bifurcation probability and branch path length are constrained by branch order, feasibly signifying that the distribution of resources overwhelms all other constraints in altered phenotypes with increased cytoplasmic resources. However, no change in optimal bf is observed, implying intrinsic maintenance of the normal connectivity patterns, even at an excess of resources. Again, the modeling predictions align well with known functions of *SkpA*, which encodes a component of the Skp, Cullin, F-box (SCF)-containing ubiquitin ligase complex. This factor has been previously shown to function in dendritic pruning of Class IV da neurons during pupal metamorphosis (Wong et al. 2013). Here, in larval development, *SkpA* knockdown leads to increased complexity, suggestive of an involvement of ubiquitin-linked proteasomal degradation in containing Class IV arborization, possibly by restricting or turning over excess cytoplasmic resources.

We also observe evidence of innate scaling of size and complexity in Class IV neurons. First, our analysis of homeostasis detected a tight interaction between stem-specific changes in length and in the number of terminals (Fig. 3e). Second, comparing WT ddaC with all ddaC mutants (Table 1) reveals that a decrease in total length is also accompanied with a reduction in total number of bifurcations, and vice versa. This shows that dendritic scaling occurs in ddaC neurons independent of RNAi knockdowns, consistent with previously observed innate dendritic scaling properties for Class IV mutants (Iyer et al. 2013).

The above results complement those obtained with a segmental rate growth model (van Pelt et al. 1997), in which local information of branch order, branch thickness or distance from the soma have no direct influence over the dynamic behavior of growth cones. Not surprisingly, a steady increase of parameter B (controlling the expected number of bifurcation in a branch) reproduced the distributions observed in progressively more complex trees structures. For example, the optimal parameter B for the *SkpA* knockdown, a phenotype with increased complexity, was much higher than ddaC *RpS2*, which has highly reduced branch complexity (18.1 vs 8.9 with WT ddaC at 15.5). Higher variability in Class III tree complexity (when compared with Class I) was reproduced with a lower value for parameter E, expressing the reduced influence of the total number of terminals at any time point over growth cone bifurcation. When comparing these results against previous analyses of dendritic arbors (van Pelt and Schierwagen 2004), E values (representing competition among individual growth cones) are in the range of many other neuron types (0.2–0.45, but not pyramidal neurons) except in the case of Class I. Parameter B is larger than many of the previous neuron types analyzed, illustrating a higher degree of intrinsic drive for branching in the *Drosophila* DA neurons.

Overall, these results support the notion that the total amount and the distributions of cytoplasmic resources play significant roles in defining arbor morphology. Unfortunately, we presently lack arbor-wide quantifications of subcellular structures regulating growth. In earlier work, we finessed this limitation by incorporating “hidden” parameters in local models (Samsonovich and Ascoli 2005). Here, we reverted to using morphological determinants of the mature shape instead of attempting to simulate the biochemical cascades underlying developmental dynamics. In particular, the interplay of growth mediator molecules such as microtubules and neurofilaments are likely to play a prominent role in this process (van Beuningen et al. 2015; Brill et al. 2016). We speculate that the microtubule to neurofilament proportion may systematically vary across and within dendritic branches, as well as between neurons groups with different optimum balancing factors. In order to test this hypothesis, and build more powerful and predictive computational models, local densities of these cytoplasmic resources have to be quantified across whole dendritic arbors. Using the arbor-wide local quantity of cytoskeletal substrates directly as determinants of growth in simulations will allow us to gain a much deeper and more reliable understanding of dendritic development.

Supplementary Material

Refer to Web version on PubMed Central for supplementary material.

Acknowledgments

The authors sincerely thank Cox Lab members Sarah G. Clark, and Atit A. Patel for the image stack generation; and Ascoli Lab members Griffin Badalamente, Alisha Compton, Anna Lulushi and Margaret Kirtley for help with neuronal reconstructions; Rubén Armañanzas for ideas and brain storming; and Diek Wheeler for critical review of the manuscript. Supported by National institute of Health: NIH NS39600, NIH NS086082, NIH MH086928, and National Science Foundation: NSF DBI1546335, and NSF BCS1663755. Stocks obtained from the Bloomington Drosophila Stock Center (NIH P40OD018537) were used in this study.

References

Ascoli GA (2002) Neuroanatomical algorithms for dendritic modeling. Network 13:247–260. doi: 10.1088/0954-898X/13/3/301 [PubMed: 12222813]

Ascoli GA, Donohue DE, Halavi M (2007) NeuroMorpho.Org: a central resource for neuronal morphologies. J Neurosci 27:9247–51. doi: 10.1523/JNEUROSCI.2055-07.2007 [PubMed: 17728438]

Ascoli GA, Krichmar JL (2000) L-Neuron: A modeling tool for the efficient generation and parsimonious description of dendritic morphology. Neurocomputing 32–33:1003–1011. doi: 10.1016/S0925-2312(00)00272-1

Bird AD, Cuntz H (2016) Optimal current transfer in dendrites. PLoS Comput Biol 12:e1004897. doi: 10.1371/journal.pcbi.1004897 [PubMed: 27145441]

Brill MS, Kleele T, Ruschkies L, et al. (2016) Branch-Specific Microtubule Destabilization Mediates Axon Branch Loss during Neuromuscular Synapse Elimination. Neuron 92:845–856. doi: 10.1016/j.neuron.2016.09.049 [PubMed: 27773584]

Burke RE, Marks WB, Ulfhake B (1992) A parsimonious description of motoneuron dendritic morphology using computer simulation. J Neurosci 12:2403–2416. [PubMed: 1607948]

Corty MM, Matthews BJ, Grueber WB (2009) Molecules and mechanisms of dendrite development in Drosophila. Development 136:1049–1061. doi: 10.1242/dev.014423 [PubMed: 19270170]

Couton L, Mauss AS, Yunusov T et al. (2015) Development of connectivity in a motoneuronal network in Drosophila larvae. Curr Biol 25:568–576. doi: 10.1016/j.cub.2014.12.056 [PubMed: 25702582]

Cuntz H, Forstner F, Borst A, Häusser M (2010) One rule to grow them all: A general theory of neuronal branching and its practical application. PLoS Comput Biol. 6(8): e1000877. doi: 10.1371/journal.pcbi.1000877 [PubMed: 20700495]

Donohue DE, Ascoli GA (2005) Models of neuronal outgrowth In: Koslow SH, Subramaniam S (eds) Databasing the Brain: From Data to Knowledge. Wiley Press, Hobokenm, NJ, 303–323

Donohue DE, Ascoli GA (2008) A comparative computer simulation of dendritic morphology. PLoS Comput Biol. 4(5):e1000089. doi: 10.1371/journal.pcbi.1000089 [PubMed: 18483611]

Feng L, Zhao T, Kim J (2015) neuTube 1.0: A new design for efficient neuron reconstruction software based on the SWC Format. eNeuro 2:ENEURO.0049–14.2014. doi: 10.1523/ENEURO.0049-14.2014

Gao FB (2007) Molecular and cellular mechanisms of dendritic morphogenesis. Curr Opin Neurobiol 17:525–532. doi: 10.1016/j.conb.2007.08.004 [PubMed: 17933513]

Grueber WB, Jan LY, Jan YN (2002) Tiling of the Drosophila epidermis by multidendritic sensory neurons. Development 129:2867–78. doi: 10.1083/jcb.140.1.143 [PubMed: 12050135]

Grueber WB, Jan LY, Jan YN (2003) Different levels of the homeodomain protein Cut regulate distinct dendrite branching patterns of Drosophila multidendritic neurons. Cell 112:805–818. doi: 10.1016/S0092-8674(03)00160-0 [PubMed: 12654247]

Hillman D (1979) Neuronal shape parameters and substructures as a basis of neuronal form In: Schmitt F (ed) The Neurosciences, 4th Study. Cambridge: MIT Press, 477–498

Iyer EPR, Iyer SC, Sullivan L et al. (2013) Functional genomic analyses of two morphologically distinct classes of Drosophila sensory neurons: post-mitotic roles of transcription factors in dendritic patterning. PLoS ONE 8(8): e72434. doi:10.1371/journal.pone.0072434 [PubMed: 23977298]

Jan YN, Jan LY (2010) Branching out: mechanisms of dendritic arborization. Nat Rev Neurosci 11:316–328. doi: 10.1038/nrn2854 [PubMed: 20404840]

Jinushi-Nakao S, Arvind R, Amikura R et al. (2007) Knot/Collier and Cut control different aspects of dendrite cytoskeleton and synergize to define final arbor shape. Neuron 56(6):963–978. doi:10.1016/j.neuron.2007.10.031 [PubMed: 18093520]

Koene RA, Tijms B, Van Hees P, et al. (2009) NETMORPH: A framework for the stochastic generation of large scale neuronal networks with realistic neuron morphologies. Neuroinformatics 7:195–210. doi: 10.1007/s12021-009-9052-3 [PubMed: 19672726]

Kole MHP, Czeh B, Fuchs E (2004) Homeostatic maintenance in excitability of tree shrew hippocampal CA3 pyramidal neurons after chronic stress. Hippocampus 14:742–751. doi: 10.1002/hipo.10212 [PubMed: 15318332]

London M, Häusser M (2005) Dendritic Computation. Annu Rev Neurosci 28:503–532. doi: 10.1146/annurev.neuro.28.061604.135703 [PubMed: 16033324]

Mainen ZF, Sejnowski TJ (1996) Influence of dendritic structure on firing pattern in model neocortical neurons. Nature 382:363–366. doi: 10.1038/382363a0 [PubMed: 8684467]

Nguyen MD, Shu T, Sanada K et al. (2004) A NUDEL-dependent mechanism of neurofilament assembly regulates the integrity of CNS neurons. Nat Cell Biol 6:595–608. doi: 10.1038/ncb1139 [PubMed: 15208636]

Parrish JZ, Emoto K, Kim MD, Jan YN (2007) Mechanisms that regulate establishment, maintenance, and remodeling of dendritic fields. Annu Rev Neurosci 30:399–423. doi: 10.1146/annurev.neuro.29.051605.112907 [PubMed: 17378766]

Peng H, Bria A, Zhou Z et al. (2014) Extensible visualization and analysis for multidimensional images using Vaa3D. Nat Protoc 9:193–208. doi: 10.1038/nprot.2014.011 [PubMed: 24385149]

Ramón y Cajal S (1995) Histology of the nervous system of man and vertebrates. New York : Oxford University Press.

Samsonovich AV, Ascoli GA (2005) Statistical determinants of dendritic morphology in hippocampal pyramidal neurons: A hidden Markov model. Hippocampus 15:166–183. doi: 10.1002/hipo.20041 [PubMed: 15390156]

Samsonovich AV, Ascoli GA (2006) Morphological homeostasis in cortical dendrites. Proc Natl Acad Sci U S A 103:1569–74. doi: 10.1073/pnas.0510057103 [PubMed: 16418293]

Scorcioni R, Polavaram S, Ascoli GA (2008) L-Measure: a web-accessible tool for the analysis, comparison and search of digital reconstructions of neuronal morphologies. Nat Protoc 3:866–76. doi: 10.1038/nprot.2008.51 [PubMed: 18451794]

Singhania A, Grueber WB (2014) Development of the embryonic and larval peripheral nervous system of Drosophila. Wiley Interdiscip Rev Dev Biol 3:193–210. doi: 10.1002/wdev.135 [PubMed: 24896657]

Strahler AN (1953) Revisions of Horton's quantitative factors in erosional terrain. Trans Am Geophys Un 34: 345.

Sulkowski MJ, Iyer SC, Kurosawa MS et al. (2011) Turtle functions downstream of Cut in differentially regulating class specific dendrite morphogenesis in Drosophila. PLoS One 6:e22611. doi: 10.1371/journal.pone.0022611 [PubMed: 21811639]

Tavosanis G (2014) The Cell Biology of Dendrite Differentiation In: Cuntz H, Remme MWH, Torben-Nielsen B (eds) The Computing Dendrite: From Structure to Function. Springer, New York, 23–40

Tripodi M, Evers JF, Mauss A, Bate M, Landgraf M (2008) Structural homeostasis: compensatory adjustments of dendritic arbor geometry in response to variations of synaptic input. PLOS Biol. 6(10):e260. doi: 10.1371/journal.pbio.0060260 [PubMed: 18959482]

Turner HN, Armengol K, Patel AA et al. (2016) The TRP channels Pkd2, NompC, and Trpm act in cold-sensing neurons to mediate unique aversive behaviors to noxious cold in Drosophila. Curr Biol 26(23):3116–3128. doi:10.1016/j.cub.2016.09.038 [PubMed: 27818173]

Turrigiano GG, Nelson SB (2004) Homeostatic plasticity in the developing nervous system. Nat Rev Neurosci 5:97–107. doi: 10.1038/nrn1327 [PubMed: 14735113]

Uemura E, Carriquiry A, Kliemann W, Goodwin J (1995) Mathematical modeling of dendritic growth in vitro. Brain Res 671:187–194. doi: 10.1016/0006-8993(94)01310-E [PubMed: 7743207]

Uylings HBM, Smit GJ and Veltman WAM (1975) Ordering methods in quantitative analysis of branching structures of dendritic trees. Adv Neurol 12: 247–254.

van Pelt J, Dityatev AE, Uylings HB (1997) Natural variability in the number of dendritic segments: model-based inferences about branching during neurite outgrowth. J Comp Neurol 387(3): 325–40. doi: 10.1002/(SICI)1096-9861(19971027)387:3<325::AID-CNE1>3.0.CO;2-2 [PubMed: 9335418]

van Pelt J, Schierwagen A (2004) Morphological analysis and modeling of neuronal dendrites. Math Biosci 188:147–55. doi: 10.1016/j.mbs.2003.08.006 [PubMed: 14766099]

van Pelt J, Uylings HBM (2002) Branching rates and growth functions in the outgrowth of dendritic branching patterns. Network 13:261–281. [PubMed: 12222814]

van Beuningen SF, Hoogenraad CC (2016) Neuronal polarity: remodeling microtubule organization. Curr Opin Neurobiol 39:1–7. doi: 10.1016/j.conb.2016.02.003 [PubMed: 26945466]

van Beuningen SFB, Will L, Harterink M, et al. (2015) TRIM46 Controls Neuronal Polarity and Axon Specification by Driving the Formation of Parallel Microtubule Arrays. Neuron 88:1208–1226. doi: 10.1016/j.neuron.2015.11.012 [PubMed: 26671463]

Vetter P, Roth A, Häusser M (2001) Propagation of action potentials in dendrites depends on dendritic morphology. J Neurophysiol 85:926–937. [PubMed: 11160523]

Wang X, Kim JH, Bazzi M et al. (2013) Bimodal control of dendritic and axonal growth by the Dual Leucine Zipper Kinase Pathway. PLoS Biol. doi: 10.1371/journal.pbio.1001572

Welch ABL (1947) The generalization of ‘Student’s’ problem when several different population variances are involved. Biometrika 34:28–35. Stable URL: http://www.jstor.org/stable/2332510 [PubMed: 20287819]

Wong JJ, Li S, Lim EK et al. (2013). A Cullin1-based SCF E3 Ubiquitin Ligase targets the InR/PI3K/TOR pathway to regulate neuronal pruning. PLoS Biol. 11(9): e1001657. doi: 10.1371/journal.pbio.1001657 [PubMed: 24068890]

Xiang Y, Yuan Q, Vogt N et al. (2010) Light-avoidance-mediating photoreceptors tile the Drosophila larval body wall. Nature 468:921–926. doi: 10.1038/nature09576 [PubMed: 21068723]

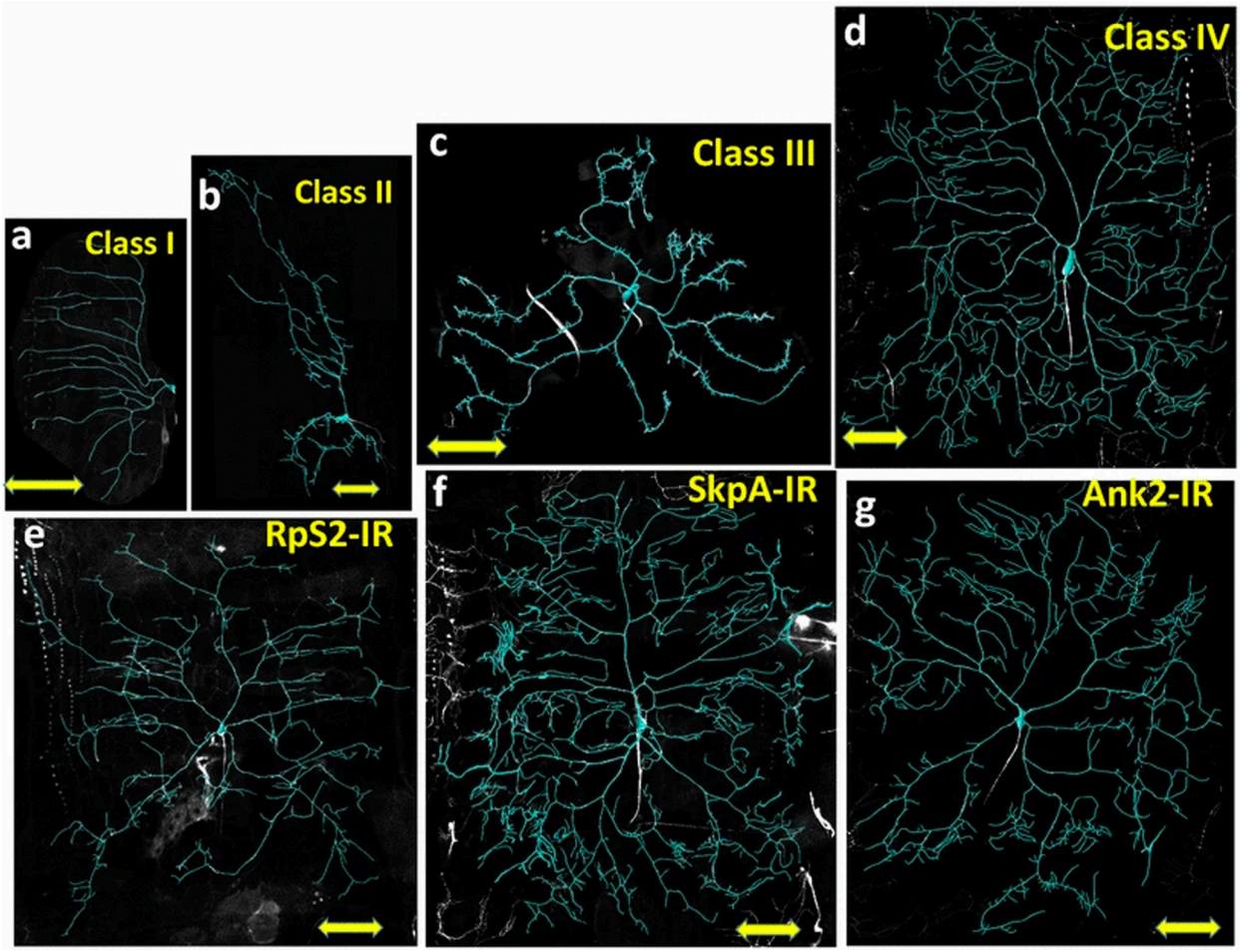

Fig. 1: Reconstructions of dendritic arborization (da) neurons, superimposed on the image stacks: three wild type (WT) cell classes and three RNA-silenced phenotypes of ddaC.

(a) Class I (ddaD); (b) Class II (ldaA) (c) Class III (v'pda); (d) Class IV (ddaC); (e) *RpS2-IR* (ddaC): reduction in complexity; (f) *SkpA-IR* (ddaC): Increase in complexity; (g) *Ank2-IR* (ddaC): Overall similar to WT ddaC, with moderate reduction in branch numbers close to the soma and tufted branching at distal dendritic terminals. All scale bars are 100 μm.

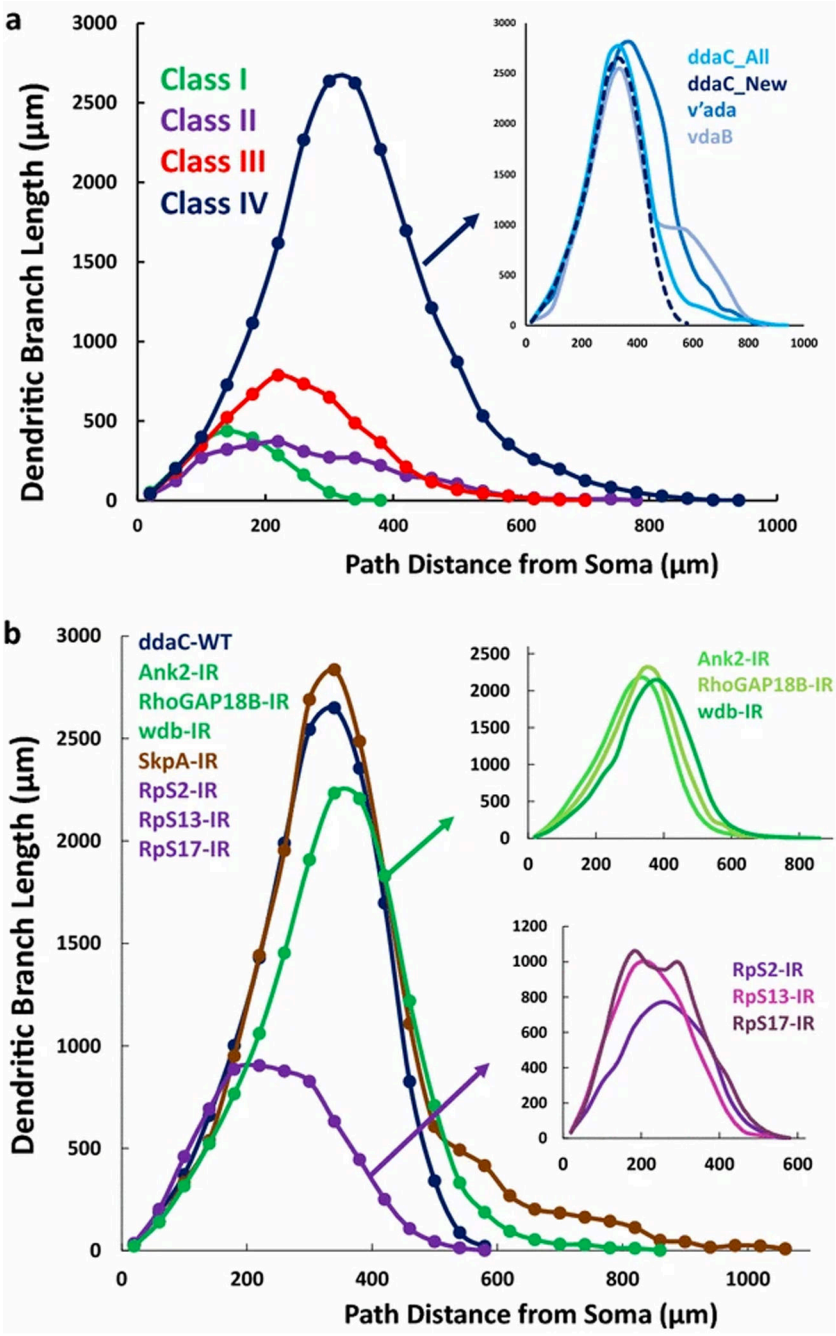

Fig. 2: Quantitative morphometry of the four wild type da neuron cell classes and of the genetically altered phenotypes of Class IV subtype ddaC.

(a) Four da neuron cell classes are compared by the distribution of dendritic length against path distance from soma. Inset: comparison of all Class IV subtypes, with the blue dotted line indicating the ddaC data newly reconstructed for this study. (b) Comparison of WT ddaC with all RNAi silenced (IR) ddaC phenotypes analyzed in the study. Inset 1 (green arrow): three IR ddaC phenotypes that are only slightly less complex than WT ddaC, but distally shifted. Inset 2 (purple arrow): three IR phenotypes with significantly reduced arbor complexity.

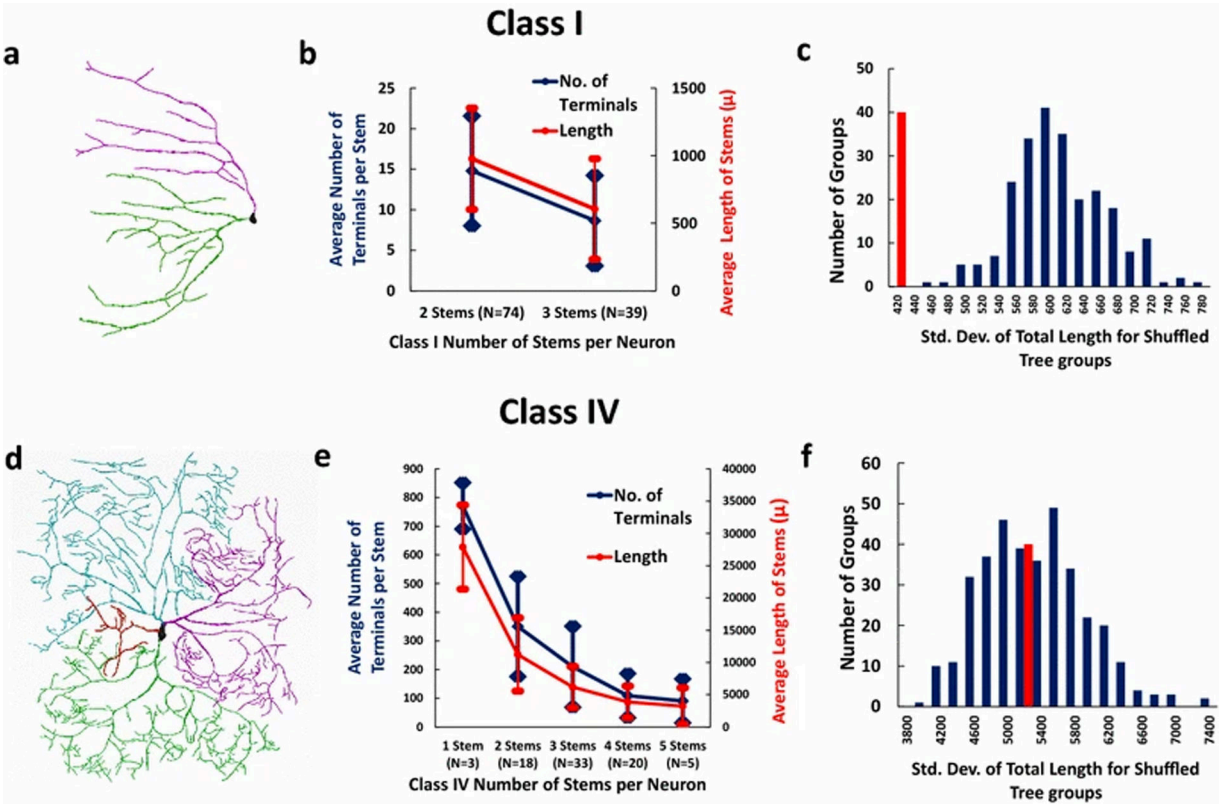

Fig. 3: Morphological homeostasis in da neurons.

(a) Reconstruction of a Class I (ddaD) neuron, with two individual stems (green and purple) of slightly different sizes, emerging from the soma. (b) Average length and average number of terminals for each dendritic stem as a function of the total number of stems in individual Class I neurons. (c) Distribution of standard deviations of the total length of artificial Class I cell groups, created by shuffling individual trees among real neurons. Trees were only shuffled among neurons with the same number of stems, and then pooled together and randomly grouped. The red bar is the standard deviation of total dendritic length in real Class I neurons. (d) Reconstruction of a Class IV (ddaC) neuron, with four individual stems (green, purple, sky-blue, and red) of different complexities, emerging from the soma. (e) Same as (b) for Class IV neurons. (f) Same as (c) for Class IV neurons.

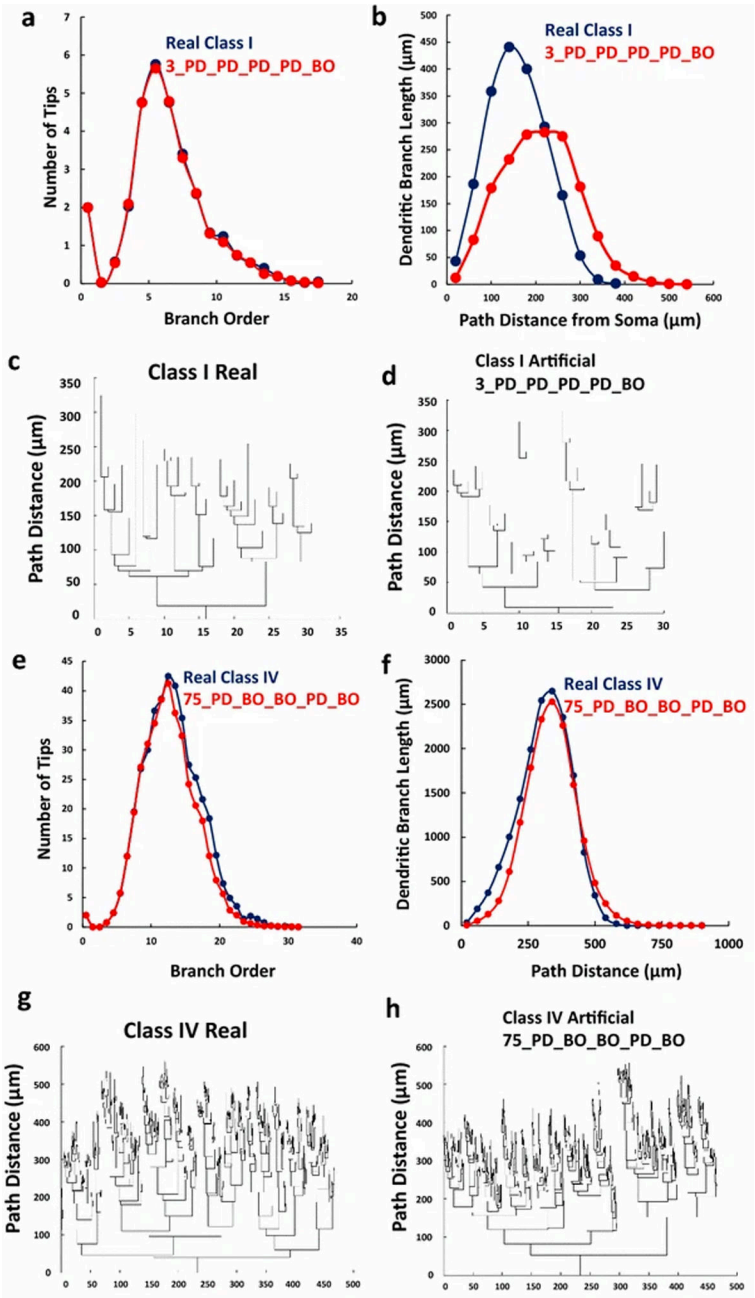

Fig. 4: Generation of artificial da neurons using local rule-based simulation.

(a) Distribution of the number of tips against branch order for real Class I neurons (blue line) and for artificial Class I neurons (red line) generated using the optimal local model variant. (b) Distribution of dendritic length against path distance from soma, for real Class I neurons (blue) and for artificial Class I neurons (red). (c) Dendrogram of a real Class I neuron. (d) Dendrogram of a simulated Class I neuron. (e) Same as (a) for Class IV neurons. (f) Same as (b) for Class IV neurons. (g) Dendrogram of a real Class IV neuron. (h) Dendrogram of a simulated Class IV neuron. The local model variant names in this figure and for all following figures describe the index of the model variant, followed by the series of FDs that constrained the five BPs (taper rate, daughter ratio, parent daughter ratio, branch path length,

bifurcation probability). PD: path distance from soma; RD: radius; BO: branch order. The terminal spacing for all dendrograms in this and subsequent figures is 1 μm; thus, X-axis approximates the total number of terminals. The dendrogram Y-axis represents path distance from soma.

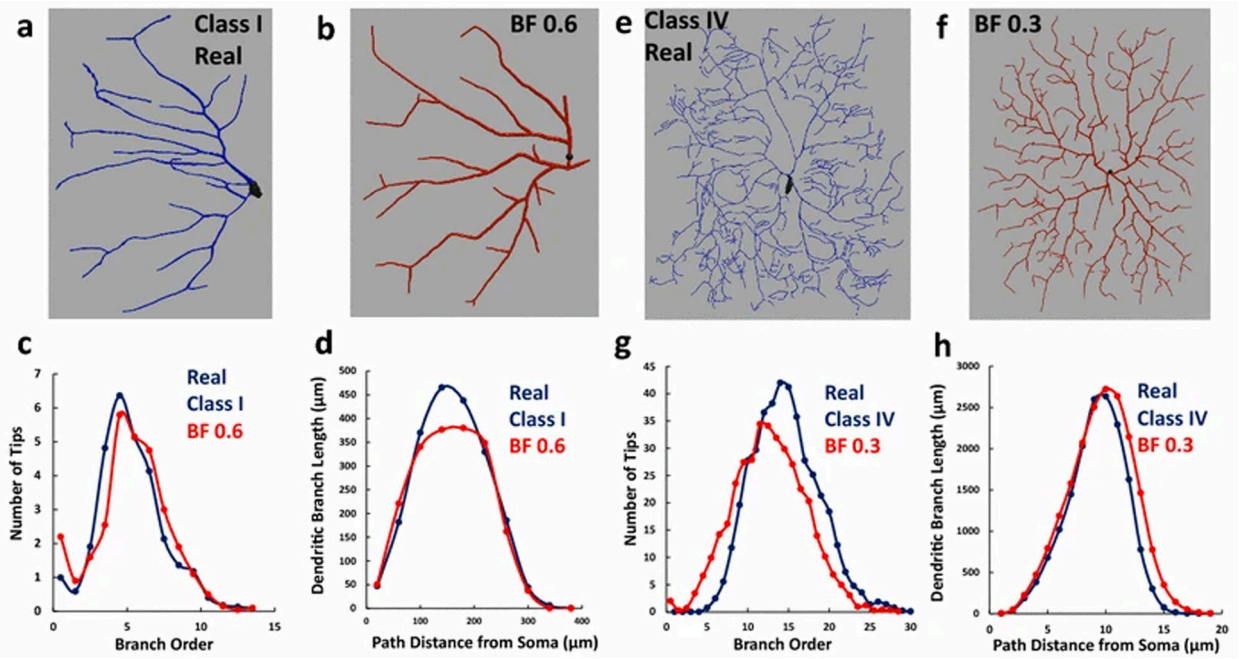

Fig. 5: Generation of artificial da neurons using global rule-based simulation.

(a) Example of a real Class I da neuron. (b) Example of an artificial Class I neuron generated using a balancing factor (bf) of 0.6. (c) Distribution of number of tips against branch order and (d) of dendritic length against path distance in real Class I neurons (blue) and artificial Class I neurons generated with a bf of 0.6 (red). (e) Example of real Class IV da neuron. (f) Example of an artificial Class IV neuron generated with a balancing factor of 0.3. (g) Distribution of the number of tips against branch order and (h) of dendritic length against path distance in real Class IV neurons (blue) and artificial Class IV neurons generated with a bf of 0.3 (red).

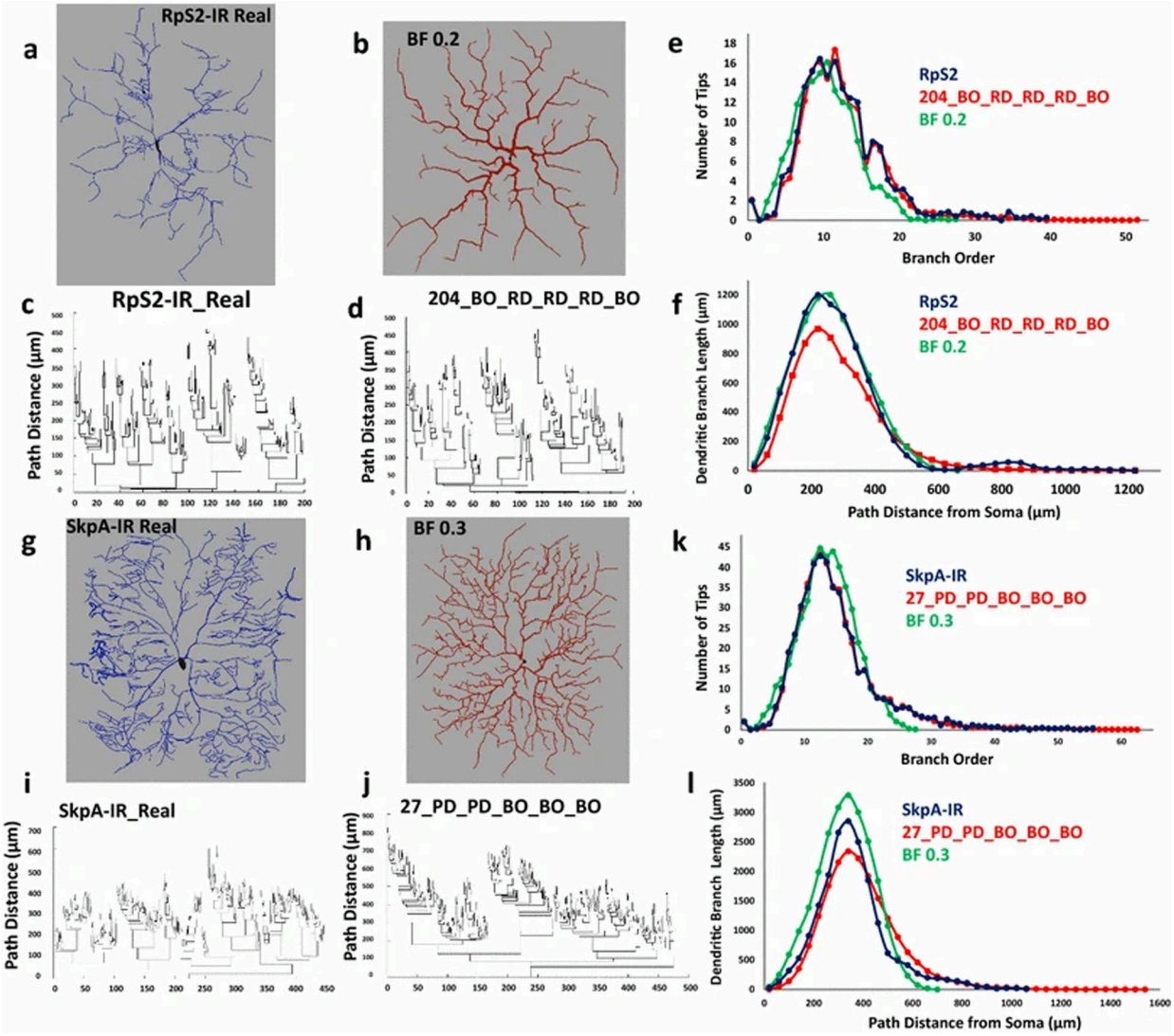

Fig. 6: Comparing the morphology of two RNA-silenced ddaC phenotypes (RpS2-IR: reduced complexity; SkpA-IR: increased complexity) using local and global rule-based simulations.

(a) Example of a real *RpS2-IR* neuron. (b) Example of an artificial *RpS2-IR* neuron generated at the balancing factor of 0.2. (c) Dendrogram of a real *RpS2-IR* neuron. (d) Dendrogram of an artificial *RpS2-IR* neuron generated using the optimal local parameters (204_BO_RD_RD_RD_BO). (e) Distribution of tips against branch order and (f) of length against path distance for real *RpS2-IR* (blue), and optimum-local (red) and optimum-global (green) artificial *RpS2-IR* neuron groups. (g) Example of a real *SkpA-IR* neuron. (h) Example of an artificial *SkpA-IR* neuron generated at the balancing factor of 0.3. (i) Dendrogram of real *SkpA-IR* neuron. (j) Dendrogram of an artificial *SkpA-IR* neuron generated using the optimal local parameters (27_PD_PD_BO_BO_BO). (k) Distribution of tips against branch order and (l) of length against path distance from soma for real *SkpA-IR* (blue), and optimum-local (red) and optimum-global (green) artificial *SkpA-IR* neuron groups.

Table 1:

Number of neurons, number of terminal tips, total dendritic length, and optimum global and local parameters of all modeled tree groups.

Neuron groups	Number of neurons	Average no of tips	Std. dev. of tips	Average total length	Std. dev. of length	Global balancing factor	Branch path length determinant	Biff prob. determinant
Class I	50	28.8	8	1919.8	419.7	0.6	PD	BO
Class II	18	112.4	28	3067	761.8	0.3	BO	BO
Class III	34	366.5	132.8	5241.9	904.4	0.0	PD	BO
Class IV	34	616.8	219	19,241	5292.8	0.3	PD	BO
Class IV ddaC								
WT	13	417.7	96.9	16,163.8	1976.9	0.3	PD	BO
RpS2-IR	7	177	79.4	8565.2	3140.3	0.2	RD	BO
RpS13-IR	6	136	26.6	6276.4	1318	0.2	BO	BO
RpS17-IR	6	150.83	23	7441.7	755	0.2	RD	PD
Ank2-IR	12	388.8	119.9	14,031.1	2745.1	0.4	PD	BO
RhoGAP18B-IR	12	382.5	51.2	14,652	1131.2	0.3	RD	BO
wdb-IR	9	374	82.9	14,643.1	1949.3	0.3	PD	BO
SkpA-IR	11	473.3	88.9	19,039	1939.1	0.3	BO	BO